Impairment of lipid homoeostasis causes accumulation of protein aggregates in the lysosome

Authors

John Yong, Jacqueline E. Villalta, Ngoc Vu, Matthew A. Kukurugya, Bryson D. Bennett, Magdalena Preciado López, Julia R. Lazzari-Dean, Kayley Hake, Calvin H. Jan

Abstract

Protein aggregation increases during aging and is a pathological hallmark of many age-related diseases. Protein homeostasis (proteostasis) depends on a core network of factors directly influencing protein production, folding, trafficking, and degradation. Cellular proteostasis also depends on the overall composition of the proteome and numerous environmental variables. Modulating this cellular proteostasis state can influence the stability of multiple endogenous proteins, yet the factors contributing to this state remain incompletely characterized. Here, we perform genome-wide CRISPRi screens to elucidate the modulators of proteostasis state in mammalian cells using a fluorescent dye to monitor endogenous protein aggregation. These screens recovered components of the known proteostasis network, and uncovered a link between protein and lipid homeostasis. We subsequently showed that increased lipid uptake and/or disrupted lipid metabolism led to increased lysosomal protein aggregation and, concomitantly, accumulation of sphingolipids and cholesterol esters. Surprisingly, lysosomal proteostasis impairment by lipid dysregulation is independent of lipid peroxidation or changes in lysosomal stability, nor is it caused by effects on many other aspects of lysosomal or proteasomal function. These results suggest that lipid dysregulation may have primary effects on the stability of endogenous proteins, potentially through direct biophysical mechanisms.

Introduction

Protein aggregation is a hallmark of aging and age-related pathologies, including multiple neurodegenerative diseases and amyloidoses that affect individual or multiple organs [1,2]. Dozens of proteins that are normally soluble may form aggregates that are traditionally associated with specific diseases -- e.g. tau tangles and amyloid plaques with Alzheimer's Disease, and transthyretin deposits with transthyretin amyloidosis [2]. Emerging evidence in the past decade or so, however, suggests a more complex relationship among different aggregation-prone proteins, either directly or through interaction with the cellular machinery regulating proteostasis. For instance, experiments in yeast, worms, and mammalian cell culture have demonstrated considerable cross-talk and cross-sensitization between classic

aggregation-prone proteins [3]. Further, many more non-disease associated proteins have been found to exhibit reduced solubility and lose their native structure during normal aging [4]. Intriguingly, these insoluble non-disease associated proteins can seed the formation of classical amyloids *in vitro*, as well as contribute to functional decline in aging animals [5]. Together, the evidence suggests that systemic changes in the state of cellular proteostasis may underlie proteinopathy, and highlights the importance of expanding the scope of studies beyond specific disease-associated protein species.

The core proteostasis network is well described and involves the synthesis, folding, trafficking and degradation of proteins [6–8]. Most of these components closely follow the life cycle of proteins, including 1) pathways that modulate protein synthesis and degradation, such as mTORC, ribosome biogenesis and processing, UPS, and autophagy; 2) molecular chaperones, which aid protein folding and refolding; and 3) stress response pathways that regulate the activity of 1) and 2) in response to accumulation of unfolded or misfolded proteins, such as ERAD and UPR. Nevertheless, the components and network topology varies depending on cell type and cell state. Furthermore, mechanisms that underlie shifts in cellular proteostasis state, especially ones that do not directly involve core nodes of the proteostasis network, remain largely unknown.

Unbiased, whole-genome screening is a powerful tool for discovering cellular components and pathways that are involved in modifying a specific phenotype. Previous studies have applied genetic screens on different cell models to uncover, for specific proteins, modifiers of their aggregation, toxicity, or propensity for aggregation to propagate from seeds. These systems are often driven by overexpression of aggregation-prone proteins and/or extracellular seeding of pre-formed fibers [9–11]. Thus, while much progress has been made in understanding the homeostasis of several discrete proteins, the mechanisms influencing the broader cellular proteostasis network remain largely unknown. In particular, we are interested in cellular mechanisms that affect the aggregation state of endogenous proteins, as these may be the most germane to age-associated loss of proteostasis.

To uncover novel components and pathways that regulate endogenous protein homeostasis, we applied CRISPR interference (CRISPRi) technology to perform unbiased, genome-wide screens on K562 cells using an aggresome-staining dye, ProteoStat. ProteoStat is known to label both experimentally induced aggresomes and aggregates that accumulate with age in the CNS of mammals [12–15]. Our screens uncovered a link between lysosomal lipid homeostasis and proteostasis. Increased levels of sphingolipid and cholesterol esters, either as a result of increased lipid uptake or decreased lysosomal degradative capacity, lead to increased protein aggregation in cells. Lipid dysregulation induces lipid peroxidation, however this was not required for lipid-induced protein aggregation. Furthermore, lipid dysregulation induces protein aggregation without compromising lysosomal membrane integrity, lysosomal protease activity, or proteasome activity. Together, this work provides strong evidence that supports an emergent role of lipid dysregulation in disrupting endogenous protein homeostasis, independent of currently known mechanisms of action.

Results

FACS-based reporter for endogenous cellular proteostasis state

ProteoStat has been used to stain endogenous protein aggregation in fixed cells. Like Thioflavin T, ProteoStat fluorescence increases when rotationally confined by binding to cross-beta sheets in amyloidal structures. The dye has recently been used in studies to visualize aggregated proteins in mouse NSCs and in *C. elegans* [12,13,15,16]. To verify that ProteoStat can be used to report changes in proteostasis in human cell cultures, we inhibited proteasomes in K562, U2OS, and A549 cells and stained them for microscopy or flow cytometry analysis. As expected, proteasome inhibition by MG132 increased ProteoStat intensity, with numerous bright puncta around the nucleus (Fig S1A). ProteoStat-high cells obtained by fluorescence-activated cell sorting (FACS) from cells treated with submaximal dose of MG132 likewise showed numerous bright puncta, whereas ProteoStat-low cells displayed diffuse staining of lower intensity, indicating that this tool can be used to report and isolate cells in different proteostasis states (Fig 1A).

Genome-wide screen for modifiers of ProteoStat recovered major known components of the proteostasis machinery

To identify modifiers of endogenous proteostasis, we performed FACS-based, pooled screens in K562 CRISPRi cells, which stably express KRAB-dCas9. Briefly, cells carrying individual sgRNAs were fixed, stained with ProteoStat, and separated by FACS, using gates that correct for correlation between staining intensity and cell size, to obtain cells with ProteoStat intensity in the top or bottom quartiles (ProteoStat-high and ProteoStat-low, respectively; Fig 1B). Illumina sequencing of processed samples allowed us to quantify the frequency of each sgRNA in each of these two populations. This experiment was performed twice, and the resulting sgRNA frequencies were analyzed using the MAGeCK package to evaluate the effect of knockdown (KD) of each gene on the proteostasis state as reported by ProteoStat staining [17].
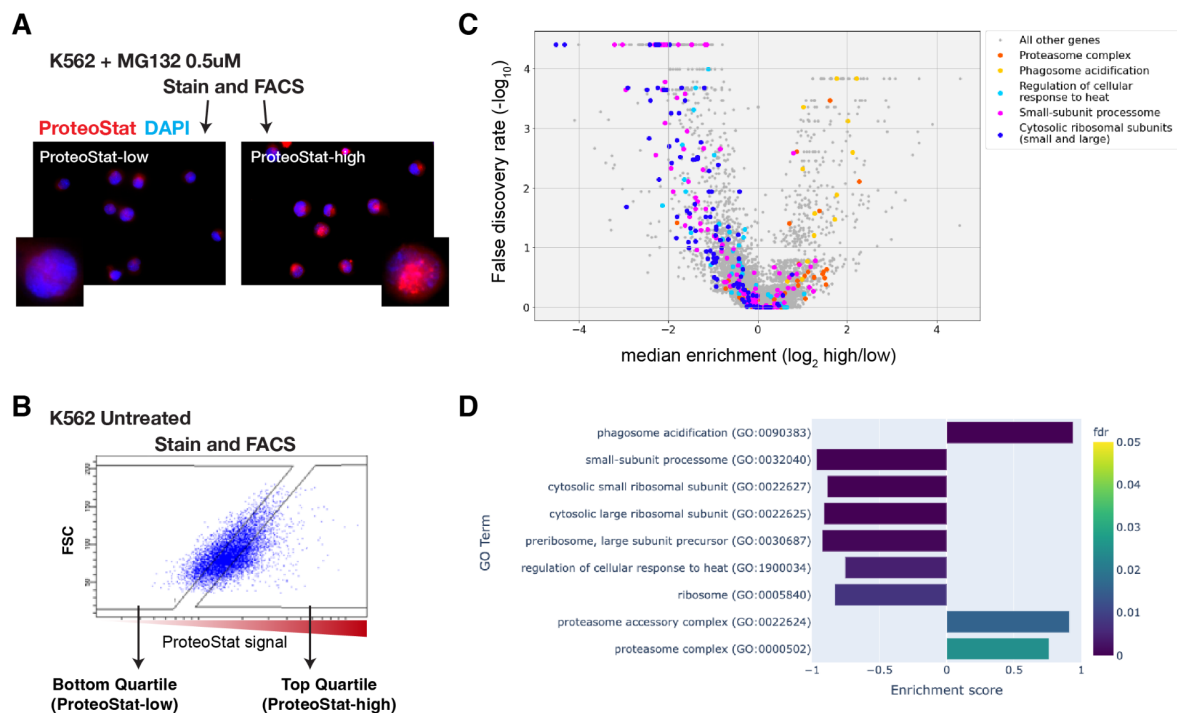
Figure 1 -- CRISPRi screens with ProteoStat recovered major cellular proteostasis components

A) MG132-treated cells (at submaximal dose) were stained, sorted into top and bottom quartiles (ProteoStat-high and ProteoStat-low, respectively), and imaged. Red: ProteoStat; Blue: Hoechst 33342. **B**) FACS schematic. Stained cells are sorted using gates that correct for correlation between staining intensity and cell size. **C**) Volcano plot visualizing CRISPRi screen results (output from MAGeCK analysis with biological duplicate experiments). Genes in select GO Terms identified with GSEA (in **D**) are highlighted. **D**) GO Terms identified with GSEA. Positive Enrichment scores indicate an increased likelihood of genes in the GO Term to increase ProteoStat phenotype when knocked-down.

The screens identified 239 genes whose KDs increased ProteoStat staining, whereas 607 genes were enriched in the ProteoStat-low population at a FDR cutoff of 0.05 (Fig 1C). The results of a select subset of genes were validated by repeating the screen at a reduced scale (batch retest; Fig S1B). We performed gene set enrichment analysis (GSEA) to capture ontologies in which genes showed consistent and significant effects in the same direction. Many of these genes and pathways were previously known to be involved in cellular proteostasis (Fig 1D). These include ribosomal proteins in both the small 40S or the large 60S ribosomal subunits, ribosome biogenesis and processing, proteasome subunits, lysosomal proton subunits (vATPases), and certain chaperones. Knocking down subunits of the proteasome complex leads to increases in ProteoStat signal, consistent with pharmacological perturbation with MG132 in our validation experiments. Similarly, disrupting vATPases increases ProteoStat staining, likely via deacidification and impairment of lysosomes, an important center where multiple catabolic processes

converge. These effects on ProteoStat signal following inhibition of the proteasome and lysosomal acidification were replicated using pharmacological inhibitors (Fig S1C). In contrast, knocking down many chaperones, including HSPA4, HSP90AB1, DNAJB6, and several subunits of TRiC chaperonins, paradoxically reduces the ProteoStat signal. Perturbing chaperones can trigger the newly described safeguard against protein aggregation mechanism that targets certain newly synthesized aggregation-prone proteins to the lysosome, notably before large visible aggregates are formed [18]. Alternatively, the paradoxical effect of chaperone inhibition on ProteoStat signal could be due to upregulation of heat shock response as a negative feedback following the initial HSP70 or HSP90 inhibition [19–21]. Indeed, pharmacological inhibition of chaperones led to increased ProteoStat signal after 30 minutes, but decreased signal after 24 hours (Fig S1C). Finally, we found that KD of many ribosomal proteins and ribosome assembly factors leads to a decrease in ProteoStat signal, consistent with reduced input of proteins into the proteostasis network [22].

Surprisingly, KD of most of the major components directly involved in macroautophagy did not lead to significant enrichment in either direction. These include the core autophagosome formation components (e.g. ATG5, ATG10, ATG12, and the ATG8 protein family) and the autophagy adaptors (NBR1, TAX1BP1, OPTN, SQSTM1 etc). Though the screens were performed under nutrient-replete conditions, CRISPRi perturbations of these genes in K562 under similar growth conditions have previously been demonstrated to influence autophagic flux [23]. These results suggest that basal autophagy plays a negligible role in clearing endogenous amyloid-like structures in this system.

Lipid uptake and metabolism modulate proteostasis

The strong association of lysosomal vATPases with Proteostat phenotype is likely due to the need to maintain a lysosomal pH of ~4.5-5.0 for optimal activity of the hydrolases that break down proteins, lipids, and nucleic acids. Failure to maintain this acidic pH can lead to lysosomal storage of undegraded macromolecules. This association prompted us to examine all lysosome-associated genes identified in the screen. We found that in addition to the vATPases, several genes that pleiotropically modulate the delivery or activity of multiple lysosomal enzymes simultaneously (e.g. GNPTAB, IGF2R, and PSAP), as well as multiple components involved in lipid uptake and metabolism (e.g. LDLR, MYLIP, and SCAP; Fig 2A) significantly affected the Proteostat phenotype. However, no perturbations of more discrete activities (e.g. individual cathepsins, lipid hydrolases or solute carriers) did so, suggesting that proteostasis is generally resilient to discrete lysosomal impairment.
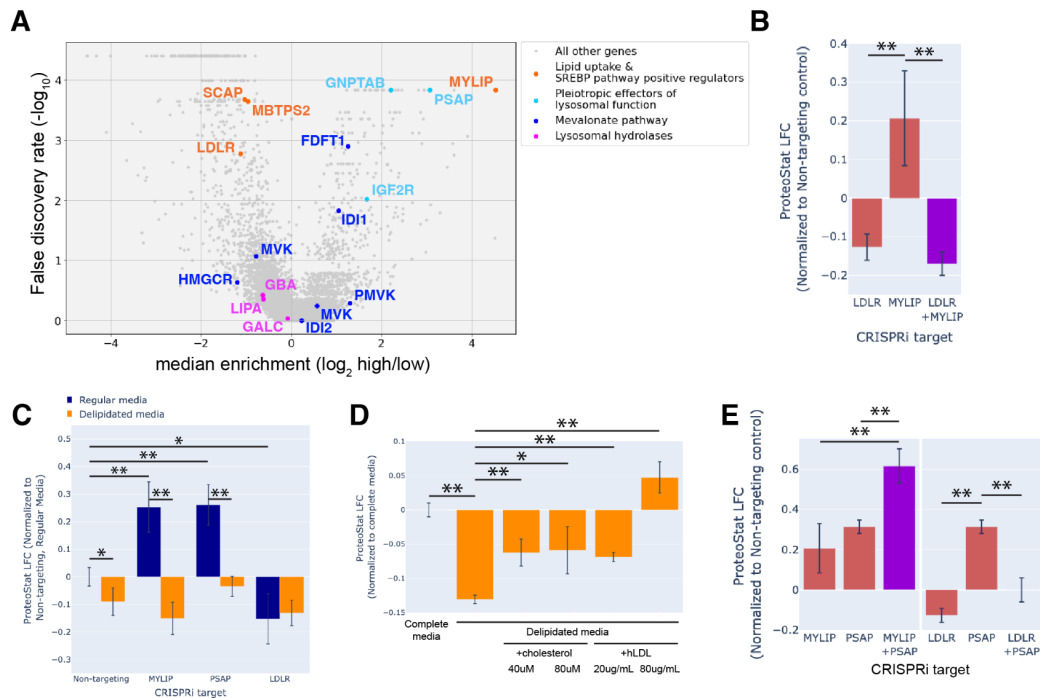
Figure 2 -- Lipid uptake and metabolism modulate proteostasis

A) Volcano plot (same as Fig 1B) highlighting select genes involved in lipid uptake and metabolism. **B & E**) Comparing effects on ProteoStat phenotypes of single-gene vs double-gene KDs (n ≥ 2) **C**) Effects of candidate gene KDs on ProteoStat phenotypes in cells maintained in media with regular or delipidated FBS for 4 days. (n = 3) **D**) Effects of supplementing free cholesterol or human LDL in rescuing the ProteoStat-lowering phenotype of cells grown in media with delipidated FBS (DL media) for 5 days (n = 3). Phenotypes in **B-E** were normalized first to an internal staining control, and then to cells infected with non-targeting guides. (✳: p<0.05; ✳✳: p<0.01; t-test)

KD of low density lipoprotein receptor (LDLR) reduced ProteoStat staining. Correspondingly, KD of the E3 ubiquitin-protein ligase MYLIP, which targets LDLR for sterol-regulated degradation, led to one of the strongest increases in ProteoStat staining. The effect of MYLIP KD on ProteoStat is via upregulated LDLR levels rather than accumulation of other MYLIP targets, as the effect of LDLR KD is epistatic to MYLIP in cells with double KD (Fig 2B). Cultured cells take up LDL - lipoproteins rich in cholesterol esters - through LDLR and the endo-lysosomal pathway. Once inside the acidic environment of the lysosomes, cholesterol ester is hydrolyzed into fatty acid and free cholesterol, the latter of which is trafficked to the ER. Excess cholesterol exerts negative feedback on LDLR levels via two mechanisms: 1) oxysterols, oxidized derivatives of cholesterol, activate the liver X receptor (LXR), in turn increasing MYLIP expression and LDLR degradation [24]; 2) high cholesterol concentration in the ER sequesters the SCAP-SREBPs complex, suppressing its activity and in turn reducing LDLR expression as well as *de novo* cholesterol synthesis [25].

A number of positive regulators of the SREBP pathways (SCAP and MBTPS2) also reduced ProteoStat staining when knocked down, though genes along the mevalonate -- *de novo* cholesterol synthesis -- pathway did not consistently score in our screen, indicating the difference between cholesterol that is taken up vs synthesized *de novo*.

Chronic depletion of exogenous LDL using media that contains delipidated serum reduces ProteoStat staining to a level similar to LDLR KD and is sufficient to abrogate the effect of MYLIP KD (Fig 2C), demonstrating that the effect of these genetic perturbations is mediated through lipid uptake and not direct degradative action of MYLIP on putative aggregation-prone substrates. Furthermore, supplementing exogenous cholesterol or human LDL either partially or completely reverses the effect of LDL depletion (Fig 2D). We also examined the possibility that ProteoStat may directly stain cholesterol by acute cholesterol extraction using methyl-β-cyclodextrin (MBCD). MBCD acutely removed most free cholesterol as determined by Filipin III staining, but did not affect ProteoStat signal (Fig S2A,B). In neither untreated nor MG132-treated cells did ProteoStat and Filipin III staining overlap, indicating that ProteoStat does not stain free cholesterol or any major components of the plasma membrane (Fig S2C). Furthermore, in an *in vitro* biphasic lipid bilayer system (giant unilamellar vesicles, GUVs), ProteoStat stained the lipid bilayer poorly and did not preferentially localize to the cholesterol-rich phase (Fig S2D). Together, the evidence suggests that increased flux of LDL uptake and/or the levels of lipid metabolites generated during the process lead to increased protein aggregation.

Our screen also implicated genes involved in lysosomal sphingolipid metabolism and lysosomal protein trafficking (Fig 2A). KD of GNPTAB, IGF2R, and prosaposin (PSAP) all led to increased ProteoStat staining. GNPTAB, a Golgi-resident enzyme, catalyzes the first step of the formation of mannose 6-phosphate (M6P) markers on lysosomal enzymes. The transport of these enzymes from the golgi to the lysosomes is facilitated by binding to M6P receptors, including IGF2R (also known as the cation-independent M6P receptor). PSAP is the precursor of saposin peptides, which are required to activate lysosomal sphingolipid catabolizing enzymes. The effect of PSAP KD was dramatically exacerbated by MYLIP KD and alleviated by LDLR KD (Fig 2E), indicating that lipid uptake can impinge on proteostasis through its interaction with lipid catabolism in the lysosome. The individual lysosomal hydrolases activated by saposins, such as GBA, GALC, and LIPA, did not rise above the detection threshold in our screen, again suggesting that proteostasis as measured by ProteoStat is generally resilient to discrete lysosomal impairment or changes in individual lipid species.

The evidence so far suggested a central role for lysosomal function in the ProteoStat phenotype under lipid-related perturbations, prompting us to further characterize ProteoStat staining, especially its subcellular localization, in reference to known biology of aggresomes. In one model of aggresome formation, misfolded and aggregated proteins are poly-ubiquitinated, transported along microtubules, and coalesced into perinuclear aggresomes, which are then detected by autophagy receptors to induce autophagosome formation, eventually delivering the cargo to the lysosomes for degradation [26]. ProteoStat

staining was initially reported to colocalize with mono-/poly-ubiquitinated proteins, p62, and LC3, and has been increasingly used as a general reporter for protein aggregation [12,13,15,16]. To our surprise, we did not see colocalization of MG132-induced ProteoStat puncta with mono-/poly-ubiquinated proteins (Fig S2E). Instead, ProteoStat puncta colocalized with lysosomes (Fig S2E,F). Lysosome-accumulating ProteoStat-positive aggregates were reported in quiescent neural stem cells but not their activated counterparts [12], nor in other rapidly dividing cell types. Together, these results suggest that ProteoStat staining revealed an unexpected subset of lysosomal protein aggregates distinct from classical aggresomes, despite comparable regulation by known proteostasis components [12,13,15,16].

Sphingolipid and cholesterol ester mediate the effect of lipid perturbations on proteostasis

The links between proteostasis and lipid metabolism, especially in the lysosomes, provoked the question of whether these changes were mediated by a small number of lipid species, or if multiple lipid species were involved. To address this question, we performed lipidomics analysis on cells in which lipid metabolism was perturbed, either genetically by CRISPRi, or environmentally by lipid depletion. These perturbations were selected from the screen results to represent a range of effects on ProteoStat staining. When only a core set of perturbations, which have direct connections with lipid uptake and metabolism, were included, we found remarkable correlation between ProteoStat staining and individual levels of most lipids in the sphingomyelin and cholesterol ester classes (R^2 of up to 0.968 and 0.843, for sphingomyelins and cholesterol esters, respectively, Fig 3A). Indeed, each of these two lipid classes -- the collection of sphingomyelins or cholesterol esters -- had significantly stronger correlation with ProteoStat phenotype when compared with the full collection of lipid compounds assayed (Fig 3B, see Fig S3A for the lipid classes ceramides (Cers), lactosylceramides (LacCers), or hexosylceramides (HexCers) as counterexamples). In contrast and for comparison, when targets that do not impinge directly on lipid metabolism (e.g. AMBRA1 or CHMP2A KD) or else expected to have strong pleiotropic effects beyond lipid metabolism (e.g. ATP6V1E1 KD) were considered, the correlation between ProteoStat staining and SM or CE lipid levels was substantially lower (insets in Fig 3A). These results further highlight the multimodality of proteostasis regulation, where lipid dysregulation represents one, among other, major components.
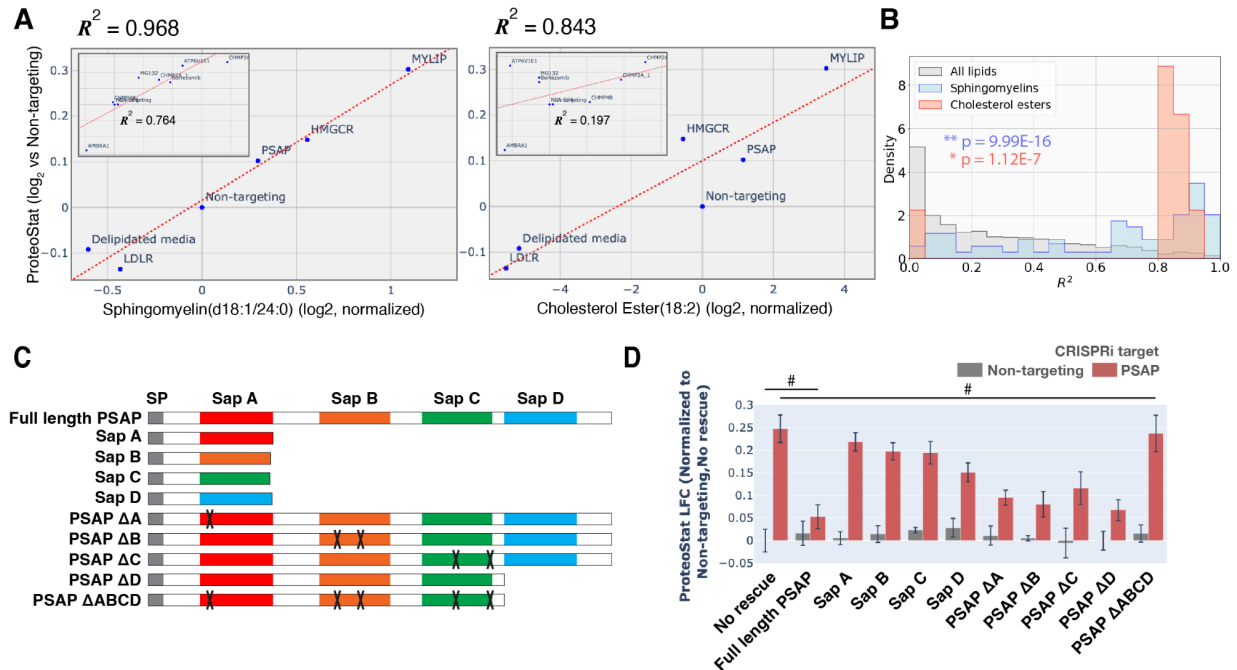
Figure 3 -- Sphingolipid and cholesterol ester mediate the effect of lipid perturbation on proteostasis

A) ProteoStat phenotype vs abundance of indicated lipid species in cells with CRISPRi KD of only a core set of lipid-related target genes, or including other ProteoStat perturbing genes (**insets**). Both ProteoStat phenotype and lipid abundance were normalized to cells carrying non-targeting guides. Least squares linear regression models (dotted red lines) were generated for the ProteoStat phenotypes and corresponding lipid abundances, and the Coefficient of determination, R^2, values for each model is shown. **B**) Histograms of R^2 values obtained for all lipid species within each indicated lipid class as in **A**. *p*-values were calculated using K-S test comparing R^2 values within each lipid class versus that of all lipids. **C**) Schematic of the series of constructs expressing different variations of PSAP (full-length, truncated, carrying mutations deleterious to individual Sap peptides, or individual functional Sap peptides alone). Colored boxes depict individual Sap peptides. Deleterious mutations are depicted by X's on the corresponding Sap peptide. **C**) ProteoStat phenotypes in cells overexpressing various PSAP variants in E, in conjunction with either PSAP KD or non-targeting control (n=3, #: p>0.05; t-test).

To determine if any lipid species alone contributes critically to protein aggregation induced by lipid dysregulation, we leveraged the modularity of the highly conserved PSAP. Upon delivery to the lysosome, the proprotein is cleaved proteolytically into four active peptides, saposins (Saps) A, B, C, and D. Saps are involved in the hydrolysis of glycosphingolipids (GSLs) as enzymatic activators, facilitating the interaction between soluble lysosomal hydrolases and GSLs embedded in the membrane [27,28]. Though homologous, distinct residues between the saposins within the saposin-hydrolase interface confer hydrolase specificity on each saposin (e.g. SapA binds to Galactocerebrosidase, GALC, and stimulates galactosylceramide hydrolysis, Fig S3B) [29]. Deficiency in full-length PSAP or individual Saps (by truncation, inactivating

mutations, or reduced expression) lead to various lysosomal storage disorders, with neuropathology and often dysfunction of other organs. Depending on which Sap is deficient, distinct GSL species are found to accumulate in the storage cells. We therefore performed rescue experiments using different PSAP variants to perturb the level of individual GSLs more specifically [30]. We created expression constructs for single Sap add-back as well as PSAPs that are full-length, truncated (Sap D deficient), or with various mutations that inactivate a single or all four Saps (Fig 3C, see Methods for a detailed description of variants). Full-length PSAP largely rescued the increase in ProteoStat level induced by PSAP KD (p=0.07 vs non-targeting control, no rescue), while the variant with all four Saps inactivated (PSAP ΔABCD) failed to rescue (p=0.74 vs PSAP KD, no rescue; Fig 3D). Furthermore, addition of any single Sap did not fully rescue the KD phenotype. Accordingly, inactivating any single Sap also did not fully abrogate PSAP's ability to rescue. Together, the evidence suggests that proteostasis impairment from sphingolipid accumulation is pleiotropic and is likely attributable to the action of multiple but not a single lipid. This is consistent with the observation that, in our CRISPRi screens, none of the individual GSL hydrolases significantly increased ProteoStat level.

Lipid perturbation affects proteostasis without gross impact on lysosomal and proteasomal functions

Sphingomyelin and cholesterol metabolism were previously linked with several diseases with proteinopathy, including Alzheimer's disease (AD) and the lysosomal storage disease Niemann Pick's type C (NPC) [30–33], yet the link between these lipid species and proteostasis remains largely unclear. We hypothesized that lysosomal function may be impaired by accumulation of sphingomyelins and cholesterol esters, as 1) the lysosome plays an important role in metabolizing cholesterol esters and sphingolipids, 2) our screen implicated lysosomal acidification as an important modulator, and 3) lysosomal phenotypes are central to various lysosomal storage diseases. Finally, multiple lines of recent evidence suggest that sphingomyelin and/or cholesterol dysregulation may induce lipid peroxidation [34,35], lysosomal membrane permeabilization (LMP) [32,36,37], and impinge on the activity of the proteasome and lysosomal proteases [33,38]. We therefore investigated different aspects of lysosomal health, including lysosomal number, size, protease activity, pH, and membrane integrity, as well as lipid peroxidation and proteasome activity, under several lipid perturbations.

To monitor lysosomal membrane integrity, we used a TagBFP-fused Galectin-3 (Gal3) reporter, which is normally diffuse in the cytoplasm, but binds to glycans on the lumenal side of lysosomal membranes that are exposed when the membrane is damaged. We imaged the reporter in cells under a combination of candidate gene KDs and/or acute LMP induced by L-leucyl-L-leucine (LLOMe), a lysosomotropic membranolytic agent (Fig 4A). CHMP2A KD, as a positive control, led to robust LMP in this assay. Unexpectedly, LDLR KD, which results in reduced CE and SM levels and reduced ProteoStat

phenotype, moderately sensitized LLOMe-induced lysosomal damage. This result can be reconciled with the observation that physiological levels of lysosomal cholesterol may protect cells against lysosomal damage [39]. In contrast, KDs of MYLIP, PSAP, and IGF2R did not affect baseline or LLOMe-induced lysosomal damage. Together, these results do not support increased LMP as an upstream determinant of protein aggregation (Fig 4B).
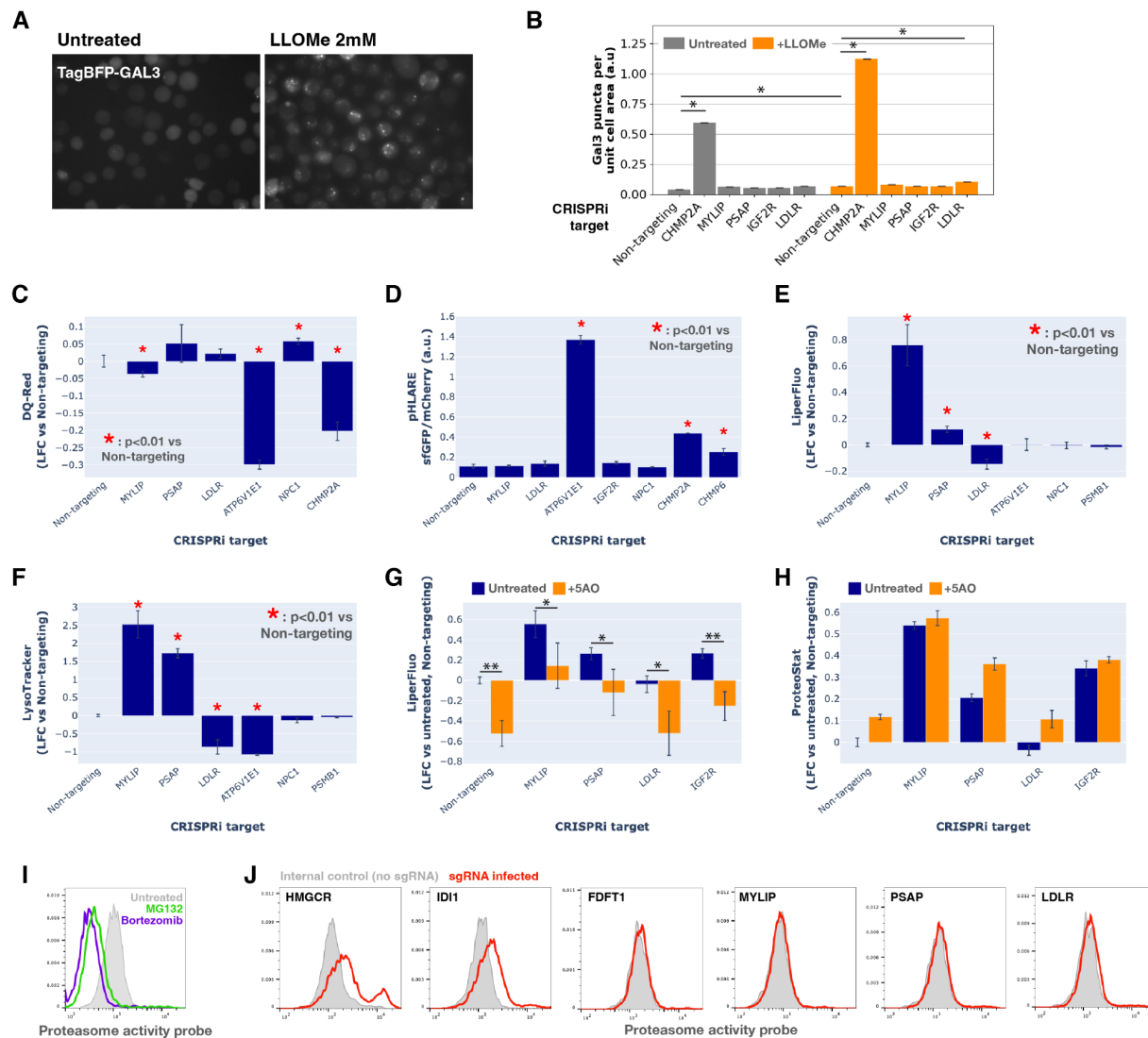
Figure 4 -- Effect of lipid perturbation on proteostasis is not mediated through the health and function of lysosomes and proteasomes

A) Representative fluorescence microscopy images of K562 cells expressing TagBFP-GAL3, either untreated or treated with LLOMe for 1.5 hours. **B**) Gal3 puncta per unit cell area quantified in fluorescence microscopy images taken with CRISPRi cells having various target gene KDs and either untreated or treated with LLOMe (n=2). **C-F**) Flow cytometry quantification of phenotypes in K562 cells with various target gene KDs. **C**: TR-X fluorescence (after protease-induced unquenching) as an indicator of lysosomal

protease function; **D**: Ratio of lysosome-targeted sfGFP fluorescence (pH sensitive) to mCherry fluorescence (pH insensitive) as an indicator of lysosomal pH; **E**: LiperFluo staining as an indicator of lipid peroxidation level; **F**: LysoTracker-Red fluorescence as an indicator of lysosomal mass and pH. **G-H**) Efficacy of the 5 antioxidant cocktail (5AO) in rescuing the effects of target gene KDs on **G**) LiperFluo or **H**) ProteoStat phenotypes. (✱: p<0.05; ✱✱: p<0.01; t-test) **I**) Flow cytometry-based assay with the Proteasome Activity Probe was validated with proteasome inhibitors. **J**) Effect of target gene KDs on proteasome activity.

To monitor lysosomal protease activity, we incubated cells with BSA conjugated to self-quenched red BODIPY TR-X (DQ-Red BSA). Uptake and delivery of these molecules to the lysosome lead to BSA hydrolysis and unquenching of the BODIPY fluorescence. As expected, impeding lysosomal acidification by ATP6V1E1 KD or lysosomal membrane integrity by CHMP2A KD led to reduced BODIPY unquenching. However, lipid-modifying perturbations affected lysosomal protease function only modestly and incoherently with respect to the ProteoStat phenotype, with MYLIP KD reducing BODIPY unquenching and PSAP KD trending in the opposite direction (Fig 4C).

Changes in lysosomal pH (pHLys) can be detected with high sensitivity using a ratiometric reporter (pHLARE), which consists of a pH-sensitive fluorescent protein (super-folder GFP, sfGFP) and a pH-insensitive one (mCherry) flanking rat LAMP1 [40]. Here, we stably expressed pHLARE, and validated the sensor for use with flow cytometry, using a buffer series with pH ranging from 4 to 7.5, in the presence of ionophores (Fig S4A). The sensor also correctly reported lysosomal deacidification as expected with ATP6V1E1 KD, and demonstrated that lysosomal membrane damage induced by either CHMP2A or CHMP6 KD led to modest increase in pHLys (Fig 4D). Nevertheless, lipid-modifying KDs -- MYLIP, PSAP, and LDLR -- did not significantly shift pHLys (Fig 4D), suggesting their effects on proteostasis are not mediated via lysosomal deacidification.

We investigated the level of lipid peroxidation and total lysosomal mass under lipid-modifying perturbations. We found that these perturbations modulate lipid peroxidation, as indicated by a fluorescent indicator, LiperFluo. Perturbations that increase or decrease sphingomyelin and cholesterol ester levels (MYLIP and PSAP KDs, vs LDLR KD) increase or decrease lipid peroxidation, respectively (Fig 4E). Interestingly, these lipid peroxidation phenotypes mirrored changes in LysoTracker intensity (Fig 4E-F, Fig S4B). As we did not observe these perturbations substantially altering pHLys (Fig 4D), the LysoTracker result suggested changes in lysosomal mass, potentially to compensate for lysosomal impairment that may or may not be a consequence of lipid peroxidation [32]. To test if lipid peroxidation is necessary for the increased protein aggregation and lysosomal mass, we supplemented the media with five antioxidants (5AO), a cocktail commonly included in the media for culturing neurons --- a cell type that is particularly sensitive to oxidative stress. However, while this antioxidant cocktail was effective in reducing lipid peroxidation, it did not rescue the Proteostat or Lysotracker phenotypes (Fig 4G-H; Fig S4C). We therefore

conclude that protein aggregation and lysosomal mass increase are likely upstream or independent of lipid peroxidation.

Finally, we investigated if the other major arm of protein catabolism -- proteasome -- is regulated by changes in lipid metabolism. A recent report suggested that high cholesterol ester levels in cells may hinder phospho-Tau degradation by proteasome inhibition [33]. We labeled active proteasomes using a fluorescent probe, Me4BodipyFL-Ahx3Leu3VS (Me4BoVS), which covalently binds to active catalytic proteasome β-subunits in live cells, and quantified the labeling by flow cytometry (Fig 4I). HMGCR KD increased proteasome activity, consistent with the reported effect of statin treatment (Fig 4J) [33]. Nevertheless, in conditions that strongly modulated sphingomyelin or cholesterol ester levels (KD of MYLIP, PSAP, or LDLR), we did not see significant increase or decrease of proteasome activity. In contrast, KD of IDI1, an enzyme downstream of HMGCR along the mevalonate pathway (but not FDFT1), strongly increased proteasome activity. We conclude that the proteasome modulating effect of statin likely arises from changes in other metabolites along the mevalonate pathway.

Discussion

Aging is associated with decreases in cellular proteostasis capacity and the accumulation of protein aggregates in diverse tissues. Despite extensive studies, factors modifying cellular proteostasis state, which has the potential to affect the state of many endogenous proteins, remain incompletely characterized. In this study, we performed genome-wide CRISPRi screens using a fluorescent dye sensitive to endogenous protein aggregation and uncovered links between lipid homeostasis and proteostasis. We discovered and characterized how changes in the uptake and metabolism of lipids, particularly sphingomyelins and cholesterol esters, lead to accumulation or depletion of these lipids and alter homeostasis of endogenous proteins.

Sphingolipid and cholesterol dysregulation has been implicated in various age-associated diseases. Intracellular sphingolipid accumulation has long been associated with lysosomal storage diseases, which share many features with age-related neurodegenerative diseases both at the level of physiology and cellular mechanism [41]. Elevated extracellular LDL cholesterol is associated with atherosclerotic cardiovascular disease [42], where modifications, including oxidation, and misfolding of apoB-100 can trigger the formation of Thioflavin T-positive fibrils of aggregated LDL and stimulate uptake by macrophages and catabolism within their lysosomes [43,44]. Consistent with our observations, MYLIP deficiency in mice leads to upregulated LDLR expression and increased cellular uptake of lipoprotein ApoE in brain tissues, but also increased uptake and clearance of extracellular aggregated Aβ peptides [45].These data affirm biological connections between lipoproteins and amyloidogenesis, the pathobiological effects of which depend on the localization of the accumulating lipids.

Prompted by the identification of lipid- and lysosome-modifying genes in altering proteostasis, we set out to understand the underlying molecular mechanism. Previously, accumulation of sphingolipid or cholesterol due to direct enzyme deficiency or impaired lipid transport was linked to reduced cellular proteostasis via impairment of lysosomal function, manifested variously as reduced lysosomal proteolytic capacity, LMP, lipid peroxidation, and aberrant mTORC1 signaling [32,38,46,47]. Surprisingly, we showed in this work that many forms of lysosomal impairment are not necessary for lipid perturbations to impinge on proteostasis. More recently, Tian and colleagues discovered in iPSC-induced neurons that PSAP KD severely impairs GSL catabolism, leading to the accumulation of these lipids and, in turn, lipofuscin formation, lipid peroxidation, and eventual cell death by ferroptosis [34]. Lipofuscins are lysosomal deposits of heterogeneous nature, consisting mainly of oxidized proteins, lipids, metal ions, and sugar residues [48]. These deposits are largely seen in post-mitotic and senescent cells, and their accumulation is observed in aged tissues but also associated with many age-related degenerative diseases [48]. Unsurprisingly, we did not observe lipofuscin in K562 cells with PSAP KD (Fig S4D), likely due to continuous dilution of damaged biomolecules by rapid cell divisions before their levels can reach a threshold to form crosslinked and undegradable granules. Despite no visible accumulation of lipofuscin, we nonetheless observed an increase in lipid peroxidation and concomitant increase in lysosomal mass, similarly to what's reported in iPSC-derived neurons [34], suggesting that granular lipofuscin formation may be dispensable for ROS generation. Furthermore, we showed that lipid peroxidation is not required for lysosomal protein aggregation induced by lipid dysregulation.

We have ruled out requirements for generalized forms of lysosomal impairment in mediating protein aggregation in our system, suggesting that aggregation may be more directly coupled to the accumulation of sphingolipids and cholesterol esters. Sterol-rich lipoproteins can promote aggregation, as in the case of LDL(-) [43], and sterols themselves can mediate solubilization of inclusion bodies in yeast [49] and lanosterol can disaggregate cataractous crystallin [50,51]. Alternatively, these lipid changes may indirectly influence the lysosomal *milieu interieur* by modulating ion channel activity [52] and changing the folding environment or altering the lysosomal proteome through changes in endolysosomal trafficking [53]. We anticipate that future elucidation of these mechanisms will contribute to our molecular understanding of protein aggregation during aging and its impact on human health.

Materials and Methods

Cell line construction and screen procedure

CRISPRi cell line was obtained by transducing K562 cells with a lentiviral vector expressing the nuclease-deactivated Cas9 fused with transcriptional repressor KRAB (UCOE-SFFV-KRAB-dCas9), followed by antibiotic selection. Monoclonal cell lines were obtained by limiting dilution, and screened

functionally for effectiveness at silencing test genes when treated with sgRNAs. Cells were maintained in suspension at a density between 125K to 1M cells/mL in RPMI complete media (with 10% FBS and 1x GlutaMax). 500 million stable CRISPRi cells were transduced with a sgRNA lentivirus pool (hCRISPRi_v2.1_top5 library, which includes 102,640 gene-targeting and 4,590 non-targeting sgRNAs) at an MOI of 0.3 for single integrants. After 6 days in culture, including antibiotic selection for cells carrying the sgRNAs with 2ug/mL puromycin, these cells were stained with fixable blue dead cell stain (Molecular Probes), then fixed, permeabilized and stained with ProteoStat Aggresome detection kit (Enzo) according to manufacturer's protocol. Stained cells were sorted by FACS (BD FACSAria) into top and bottom quartiles (ProteoStat-high and ProteoStat-low, respectively), using gates that excluded dead cells and corrected for correlation between cell size and staining intensity. Sorted cell populations were pelleted, from which genomic DNA was extracted with phenol:chloroform:isoamyl alcohol and ethanol precipitation. sgRNA-containing sequences were amplified from the genomic DNA with two rounds of PCR, introducing multiplexing barcodes and sequencing adaptors in the process. Amplicons were then purified and sequenced with the HiSeq4000 platform (Illumina). Sequencing data were analyzed using the MAGeCK pipeline [17]. GSEA was performed using the GSEAPY package [54,55].

Validation of hit genes by batch-retesting a reduced pool of CRISPRi guides

A subset of sgRNAs were selected and cloned into a reduced-scale library that consisted of 572 sgRNAs targeting 286 genes (87 enriched in ProteoStat-high, 99 enriched in ProteoStat-low, and 100 unenriched but abundantly expressed in K562 cells) and 300 non-targeting sgRNAs. sgRNA transduction in K562 CRISPRi cells, ProteoStat staining, FACS, library preparation and sequencing were performed similarly to the genome-wide experiment, except at a reduced scale (20 million cells transduced with sgRNA lentivirus pool, and >2.8 million cells each of ProteoStat-high and ProteoStat-low populations were obtained by FACS).

ProteoStat assays on cells with individual perturbations

K562 cells in multi-well plates were treated with individual perturbations and harvested for ProteoStat staining. To control for cell density-dependent variation in staining, harvested cells were spiked with untreated cells carrying appropriate fluorescent markers (e.g. TagBFP, mCerulean, or unlabeled, to be distinguished from treated cells) before fixation, permeabilization, and staining. ProteoStat fluorescence was quantified by flow cytometry (Fortessa, BD) with excitation at 488 nm and bandpass emission at 695/40 nm. ProteoStat intensity for each sample was first normalized to the internal spiked in (untreated) control, then to the corresponding negative control sample in the experiment (e.g. Non-targeting sgRNA). Individual perturbations were achieved by CRISPRi (sgRNA lentiviruses) or pharmacological inhibitors -- MG132 (EMD Millipore; 474790), Bafilomycin A1 (Invivogen; TLRL-BAF1), VER155008 (Selleckchem;

S7751), Ganetespib (Selleckchem; S1159), 17-DMAG (Invivogen; ant-dgl), MBCD (Sigma; C4555), Bortezomib (Selleckchem; S1013), LLOMe (MedKoo; 597431), and Cumene Hydroperoxide (Sigma-Aldrich; 247502). Lipid deprivation was performed by substituting regular FBS with delipidated FBS (Lipoprotein depleted FBS, Kalen Biomed; 880100).

Immunofluorescence and cell staining by fluorescent probes

Cholesterol quantification was performed by formaldehyde fixing and staining cells with Filipin III (Abcam; ab133116) according to manufacturer's instructions.

Immunofluorescence assays were performed with standard protocol. Briefly, cells were washed with PBS and fixed with 4% formaldehyde for 30 minutes at room temperature, then washed with PBS. Cells were permeabilized in blocking buffer (PBS +0.5% Triton-X 100 +5% goat serum) for 1 hour at room temperature, followed by incubating with blocking buffer + primary antibody at 4ºC overnight. Cells were then washed 3 times with PBS-T (PBS + 0.05% v/v tween20) at room temperature and incubated with blocking buffer + secondary antibody at room temperature for 1 hour. Cells were washed twice more with PBS-T and once with PBS before imaging. If co-staining with ProteoStat, the dye was included at 1:10000 during both primary and secondary antibody incubation. List of antibodies used: mouse-anti-LAMP1 (Abcam; ab25630), mouse-anti-mono/polyubiquitinated proteins (Enzo; BML-PW8810-0100), and Alexa Fluor Plus 647-conjugated goat-anti-mouse (Invitrogen; A32728).

Lipid peroxidation was quantified by incubating cells with Liperfluo (Dojindo Molecular Technologies; L24810) at 5uM for 1 hour at 37ºC. Cells were resuspended in cold PBS before analysis with flow cytometry (Fortessa, BD). Antioxidants, when included, consist of the following components at the corresponding final concentration: 5 ug/mL catalase (Sigma-Aldrich; C40), 2 ug/mL glutathione (Sigma-Aldrich; G6013), 15 U/mL superoxide dismutase (Sigma-Aldrich; S5395), 2 ug/mL DL-alpha tocopherol (Sigma-Aldrich; T3251), and 2 ug/mL DL-alpha tocopherol acetate (Sigma-Aldrich; T3001).

Lysosomal protease activity was monitored with DQ-Red BSA (Invitrogen; D12051). K562 CRISPRi cells carrying sgRNAs targeting corresponding genes (7 days after sgRNA introduction) were pelleted and resuspended in prewarmed trafficking media (RPMI + 1% serum + 1% GlutaMax + 10 nM HEPES) containing 10 ug/mL DQ-Red BSA and returned to incubator at 37ºC. After incubation for 1 hour, cells were washed once with cold PBS, resuspended in cold PBS, and analyzed by flow cytometry (Fortessa, BD) with excitation at 561 nm and bandpass emission at 610/20 nm.

Lysosomal mass was estimated by incubating cells under various genetic perturbations (7 days after sgRNA transduction) with LysoTracker Red DND-99 at 100 nM (Invitrogen; L7528). After incubation at 37ºC for 1 hour, cells were washed once with cold PBS, resuspended in cold PBS, and analyzed by flow cytometry (Fortessa, BD) with excitation at 561 nm and bandpass emission at 610/20 nm.

Proteasome activity was assessed similarly by incubating cells with genetic (7 days) or chemical (1 hour) perturbations with Me4BoVS (R&D system; I-190-050). After incubation at 37ºC for 2 hours, cells were washed once with cold PBS, resuspended in cold PBS, and analyzed by flow cytometry (Fortessa, BD) with excitation at 488 nm and bandpass emission at 525/50 nm.

Lipidomics experiment and data analysis

K562 cells under various CRISPRi or lipid perturbations were maintained, in triplicate, for 7 days. Cells were pelleted, resuspended in fresh medium, and returned to culture on Day 6 -- one day before up to ~ 1 million cells per sample were harvested. Briefly, cells were pelleted and washed twice with PBS at 4ºC, then lysed using 800 uL of ice-cold MeOH:H2O (1:1,v/v) containing 3% by volume of lipid standards - Avanti 330707 SPLASH® LIPIDOMIX® Mass Spec Standard) at -20ºC, and transferred to a glass vial. Following the methanol-tert-butyl methyl ether Matyash extraction method [56], 800 uL of 100% MTBE was added into each sample, vortexed, and incubated on ice for 10 minutes to form phase separation. Next, after centrifuging samples at 3500RPM at 4°C for 5 minutes, 500 uL of the upper organic phase was collected into a clean glass vial, and the lower phase was re-extracted by the addition of 600 uL of 100% MTBE as described above. The organic phases were combined, dried under nitrogen, and resuspended in 150 uL of HPLC graded-ButOH/MeOH/H2O (2:2:1,v/v/v) with internal standards including: 5 ug/mL PE(18:0/18:0)-D70, PA(14:0/14:0)-D54, and 25 ug/mL LPC (16:0)-D31. Samples were analyzed using Thermo Scientific Vanquish UHPLC coupled with Q Exactive Plus Mass Spectrometer with 7.5 uL injection volume.

Analysis was done in both negative and positive mode ionization with separation on a Thermo Accucore C30 (250 x 2.1 mm, 2.6 µm polymer particles). Mobile phase A was 20 mM ammonium formate in MeCN:water (60:40,v/v); mobile phase B was 20 mM ammonium formate in isopropanol:MeCN (90:10, v/v) and a flow rate of 0.2 mL/min was used. The column was equilibrated for 7 min in 30% B prior to injection; followed by a gradient of 30-43%B from 0 to 7 min, 43-65% B from 7 to 12 min, 65-70% B from 12 to 30 min, 88% B at 31 min, 88-95% B at 51 min, 100% B at 53 min and 55 min, and 30%B from 55 to 60 min.

The source parameters were as follows: Sheath gas: 40; Aux gas:15; Sweep gas: 1; spray voltage 3.1 kV, the capillary temperature of 275°C, and S-lens RF level of 50. The mass spectrometer was operated in data-dependent top-8 MS2 mode, with 14000 resolution setting and AGC of 3e6 for MS1, and 17,500 resolution setting and AGC target of 3e6 for MS2. Stepped, normalized collision energies of 20, 30, 40 were used.

Data were analyzed and visualized using the open source software MAVEN peak analysis program (https://github.com/eugenemel/maven) [57]. Compounds were identified by comparison against an *in silico* generated lipid library of fragmentation patterns.

PSAP variant series and rescue experiments

A series of constructs expressing various PSAP variants were built into lentiviral vectors under a UBC promoter. The canonical sequence mRNA variant 1 (NM_002778.4) was designated as wild-type. The full-length, wild-type sequence was modified using the following known disease-associated mutations to generate deficient variants: SapA-deficiency (p.V70del), SapB-deficiency (p.N215H_C241S), SapC-deficiency (p.L349P_C388F). The SapD-deficiency variant was created by truncating the entire C-terminal starting at the first SapD residue (p.405_524del).

PSAP KD rescue experiments were performed by co-transducing K562 CRISPRi cells with lentiviruses expressing either a PSAP-targeting or non-targeting sgRNA, and in parallel one of the various PSAP variants. Transduced cells were selected with 2 ug/mL puromycin and 500 ug/mL geneticin for doubly transduced cells. Cells were harvested 6 days after transduction, spiked with untreated cells as internal control, then stained with ProteoStat and analyzed with flow cytometry as in other experiments.

Lysosomal membrane permeability assay

Stable LMP reporter cells were generated by transducing K562 CRISPRi cells with a lentiviral vector expressing TagBFP-Gal3, followed by selection with 10 ug/mL blasticidin. To measure the effect of gene KDs on LMP, these reporter cells were transduced with corresponding sgRNA-expressing lentiviruses and selected with 2 ug/mL puromycin. 5 days after sgRNA transduction, cells were plated on poly-D-lysine-coated CellCarrier Ultra 96-well plates (Perkin Elmer) at 12K cells in 200 uL regular media per well. 2 days after plating, cells were treated with 60 uM LLOMe (or left untreated) and imaged on Opera Phenix imaging platform (Perkin Elmer) at 15-minute intervals for 4 hours, with excitation laser at 375 nm and bandpass emission filter at 435-550 nm. Images were analyzed with Harmony software (Perkin Elmer) by cell segmentation and spot detection. The number of Gal3 puncta in each field of view (6 fields per condition) is normalized by the total segmented cell area and scaled to match the average cell area, to correct for cell density and averaged across replicates. The maximal response for each sample over the 4-hour time course was reported.

pHLys quantification by pHLARE

Stable pHLys reporter cells were generated by transducing K562 CRISPRi cells with a lentiviral vector expressing pHLARE (a fusion protein consisting of prolactin signal sequence, superfolder GFP [sfGFP], rat LAMP1, and mCherry developed by Webb et al.)[40], and selected with 10 ug/mL blasticidin.

For validation, reporter cells were pelleted at 500 g for 5 minutes and resuspended in a buffer series at pHs ranging from 4 to 7.5 (140 mM KCl, 1 mM MgCl2, 1 mM CaCl2, 5 mM glucose and 10% citrate-phosphate-borate buffer at the target pH)[58] in the presence of ionophores (10 uM nigericin, 2 uM

monensin). Non-reporter cells were treated in parallel to correct for changes in background autofluorescence under various perturbations. After incubation at 37ºC for 10 minutes, cells were analyzed with flow cytometry (Fortessa, BD), using excitation-bandpass emission settings of 488 nm-525/50 nm and 561 nm-610/20 nm for sfGFP and mCherry, respectively. To elucidate the effect of gene KDs on pHLys, CRISPRi cells with or without stable pHLys reporter were transduced with sgRNA-expressing lentiviruses, selected with 2 ug/mL puromycin, and analyzed similarly with flow cytometry, 7 days after sgRNA transduction.

Cytometry data were analyzed in the FlowJo software (BD). Median background fluorescence in each channel in the cognate non-reporter controls was subtracted from the sfGFP and mCherry fluorescence intensities in the pHLys reporter samples, and the ratio of adjusted sfGFP intensity vs adjusted mCherry intensity was reported.

Giant unilamellar vesicles (GUVs) and ProteoStat staining

GUVs with binary mixtures of saturated and unsaturated lipids were obtained by electroformation. Briefly, DOPC, DPPC, and free cholesterol were mixed in equal molar parts to a final concentration of 1mg/mL. TopFluor Cholesterol (Avanti Polar Lipids Inc.) was included at 1% of total lipids. The lipid mix was spread onto ITO-coated glass coverslips and dried overnight under vacuum. Dried lipids were hydrated with 300-400 ul of a 100 mM sucrose solution while applying a sinusoidal voltage (1.2 Vp-p and 10Hz) for one hour at 60ºC. GUVs were harvested, diluted 20-fold in 200 uL of a 100 mM glucose solution supplemented with either no ProteoStat, or ProteoStat at a final dilution of 10,000x and 500x and imaged at 30ºC in a spinning disk confocal fluorescence microscope (Nikon), using excitation/emission at 488 nm/525±18 nm (TopFluor) or 561 nm/605±35 nm (ProteoStat). Multi-channel single-plane images were acquired using NIS-Elements software and analyzed with ImageJ/Fiji [59].

Transmission Electron Microscopy

K562 CRISPRi cells carrying either non-targeting or PSAP-targeting sgRNA (6 days after sgRNA transduction) were fixed by directly mixing cells in suspension 1:1 with prewarmed 1x fixative (2% glutaraldehyde and 4% paraformaldehyde in 0.1 M sodium cacodylate buffer, pH7.4), followed immediately by gentle pelleting at 100 g for 10 minutes. Cell pellets were resuspended gently with fresh 1x fixative, and incubated at room temperature for 1 hour, followed by washing once with 2 mL 0.1 M sodium cacodylate buffer at room temperature and then transferring to 0.5 mL 0.1 M sodium cacodylate buffer, each time pelleting at 100 g for 10 minutes.

Fixed cells were stored at 4ºC until they were enrobed in gelatin and post-fixed with 1% osmium tetroxide, washed with ddH$_2$O and stained with 1% uranyl acetate. Stained samples were dehydrated in a graded

series of ethanol, infiltrated and embedded in epon resin. Samples were then trimmed and sectioned with an ultramicrotome and imaged on a JEM-1400 transmission electron microscope (JEOL).

Acknowledgements

References

1. Eisenberg, D. & Jucker, M. The Amyloid State of Proteins in Human Diseases. *Cell* **148**, 1188–1203 (2012).
2. Chiti, F. & Dobson, C. M. Protein Misfolding, Amyloid Formation, and Human Disease: A Summary of Progress Over the Last Decade. *Annu Rev Biochem* **86**, 27–68 (2017).
3. Gidalevitz, T., Ben-Zvi, A., Ho, K. H., Brignull, H. R. & Morimoto, R. I. Progressive disruption of cellular protein folding in models of polyglutamine diseases. *Science* **311**, 1471–1474 (2006).
4. David, D. C. *et al.* Widespread Protein Aggregation as an Inherent Part of Aging in C. elegans. *Plos Biol* **8**, e1000450 (2010).
5. Huang, C. et al. Intrinsically aggregation-prone proteins form amyloid-like aggregates and contribute to tissue aging in Caenorhabditis elegans. *Elife* **8**, e4305**9** (2019).
6. Hipp, M. S., Kasturi, P. & Hartl, F. U. The proteostasis network and its decline in ageing. *Nat Rev Mol Cell Bio* **20**, 421–435 (2019).
7. Labbadia, J. & Morimoto, R. I. Repression of the Heat Shock Response Is a Programmed Event at the Onset of Reproduction. Mol Cell **59**, 639–650 (2015).
8. Kaushik, S. & Cuervo, A. M. Proteostasis and aging. *Nat. Med.* **21**, 1406–1415 (2015).
9. Kramer, N. J. et al. CRISPR-Cas9 screens in human cells and primary neurons identify modifiers of C9orf72 dipeptide repeat protein toxicity. *Nat Genet* **50**, 603–612 (2018).
10. Chen, J. J. et al. Compromised function of the ESCRT pathway promotes endolysosomal escape of tau seeds and propagation of tau aggregation. 9, 1825–25 (2019).
11. Willingham, S., Outeiro, T. F., DeVit, M. J., Lindquist, S. L. & Muchowski, P. J. Yeast genes that enhance the toxicity of a mutant huntingtin fragment or alpha-synuclein. *Science* **302**, 1769–1772 (2003).
12. Leeman, D. S. et al. Lysosome activation clears aggregates and enhances quiescent neural stem cell activation during aging. Science **359**, 1277–1283 (2018).
13. Shen, D. et al. Novel Cell- and Tissue-Based Assays for Detecting Misfolded and Aggregated Protein Accumulation Within Aggresomes and Inclusion Bodies. *Cell Biochem Biophys* **60**, 173–185 (2011).
14. Gefen, T. et al. Morphometric and Histologic Substrates of Cingulate Integrity in Elders with Exceptional Memory Capacity. *J Neurosci* **35**, 17**8**1–1791 (2015).
15. Vonk, W. I. M. et al. Differentiation Drives Widespread Rewiring of the Neural Stem Cell Chaperone Network. Mol Cell 78, 329-**34**5.e9 (2020).
16. Bohnert, K. A. & Kenyon, C. A lysosomal switch triggers proteostasis renewal in the immortal C. elegans germ lineage. *Nature* **551**, 629–633 (2017).
17. Li, W. et al. MAGeCK enables robust identification of essential genes from genome-scale

CRISPR/Cas9 knockout screens. *Genome Biol* **15**, 819–12 (2014).

18. Jung, R. et al. Tissue-specific safety mechanism results in opposite protein aggregation patterns during aging. *Biorxiv* 2020.12.04.409771 (2020) doi:10.1101/2020.12.04.409771.

19. Kijima, T. et al. HSP90 inhibitors disrupt a transient HSP90-HSF1 interaction and identify a noncanonical model of HSP90-mediated HSF1 regulation. *Sci Rep-uk* **8**, 6976 (2018).

20. Åkerfelt, M., Morimoto, R. I. & Sistonen, L. Heat shock factors: integrators of cell stress, development and lifespan. Nat Rev Mol Cell Bio 11, 545–555 (2010).

21. Ali, A., Bharadwaj, S., O'Carroll, R. & Ovsenek, N. HSP90 Interacts with and Regulates the Activity of Heat Shock Factor 1 in Xenopus Oocytes. *Mol Cell Biol* **18**, 4949–4960 (1998).

22. Stein, K. C. & Frydman, J. The stop-and-go traffic regulating protein biogenesis: How translation kinetics controls proteostasis. *J Biol Chem* **294**, 2076–2084 (2019).

23. Shoemaker, C. J. et al. CRISPR screening using an expanded toolkit of autophagy reporters identifies TMEM41B as a novel autophagy factor. *PLoS Biol* **17**, e2007044-31 (2019).

24. Zelcer, N., Hong, C., Boyadjian, R. & Tontonoz, P. LXR Regulates Cholesterol Uptake Through Idol-Dependent Ubiquitination of the LDL Receptor. Science **325**, 100–104 (2009).

25. Goldstein, J. L., DeBose-Boyd, R. A. & Brown, M. S. Protein Sensors for Membrane Sterols. Cell **124**, 35–46 (2006).

26. Kocaturk, N. M. & Gozuacik, D. Crosstalk Between Mammalian Autophagy and the Ubiquitin-Proteasome System. *Front. Cell Dev. Biol.* **6**, 712–27 (2018).

27. Kolter, T. & Sandhoff, K. PRINCIPLES OF LYSOSOMAL MEMBRANE DIGESTION: Stimulation of Sphingolipid Degradation by Sphingolipid Activator Proteins and Anionic Lysosomal Lipids. *Cell Dev Biology* **21**, 81–103 (2005).

28. Xu, Y.-H., Barnes, S., Sun, Y. & Grabowski, G. A. Multi-system disorders of glycosphingolipid and ganglioside metabolism. *J Lipid Res* **51**, 1643–1675 (2010).

29. Hill, C. H. et al. The mechanism of glycosphingolipid degradation revealed by a GALC-SapA complex structure. *Nat Commun* **9**, 151 (2018).

30. Schulze, H. & Sandhoff, K. Lysosomal Lipid Storage Diseases. *Csh Perspect Biol* **3**, a004804 (2011).

31. Yamazaki, T., Chang, T. Y., Haass, C. & Ihara, Y. Accumulation and aggregation of amyloid beta-protein in late endosomes of Niemann-pick type C cells. J Biol Chem **276**, 4454–4460 (2001).

32. Kirkegaard, T. et al. Hsp70 stabilizes lysosomes and reverts Niemann–Pick disease-associated lysosomal pathology. Nature **463**, 5**4**9–553 (2010).

33. Kant, R. van der et al. Cholesterol Metabolism Is a Druggable Axis that Independently Regulates Tau and Amyloid-β in iPSC-Derived Alzheimer's Disease Neurons. *Cell Stem Cell* **24**, 363-375.e9 (2019).

34. Tian, R. et al. Genome-wide CRISPRi/a screens in human neurons link lysosomal failure to ferroptosis. *Nat Neurosci* **24**, 1020–1034 (2021).

35. Choi, S.-H., Sviridov, D. & Miller, Y. I. Oxidized cholesteryl esters and inflammation. *Biochimica Et Biophysica Acta Bba - Mol Cell Biology Lipids* **1862**, 393–397 (2016).

36. Dielschneider, R. F. et al. Lysosomotropic agents selectively target chronic lymphocytic leukemia cells due to altered sphingolipid metabolism. *Leukemia* **30**, 1290–1300 (2016).

37. Petersen, N. H. T. et al. Transformation-Associated Changes in Sphingolipid Metabolism Sensitize Cells to Lysosomal Cell Death Induced by Inhibitors of Acid Sphingomyelinase. *Cancer Cell* **24**, 379–393 (2013).

38. Gabandé-Rodríguez, E., Boya, P., Labrador, V., Dotti, C. G. & Ledesma, M. D. High sphingomyelin levels induce lysosomal damage and autophagy dysfunction in Niemann Pick disease type A. *Cell Death Differ* **21**, 864–875 (2014).

39. Appelqvist, H. et al. Sensitivity to Lysosome-Dependent Cell Death Is Directly Regulated by Lysosomal Cholesterol Content. *Plos One* **7**, e50262 (2012).

40. Webb, B. A. et al. pHLARE: a new biosensor reveals decreased lysosome pH in cancer cells. *Mol Biol*

Cell **32**, 131–142 (2021).

41. Lloyd-Evans, E. & Haslett, L. J. The lysosomal storage disease continuum with ageing-related neurodegenerative disease. *Ageing Res Rev* **32**, 104–121 (2016).

42. Mortensen, M. B. & Nordestgaard, B. G. Elevated LDL cholesterol and increased risk of myocardial infarction and atherosclerotic cardiovascular disease in individuals aged 70–100 years: a contemporary primary prevention cohort. *Lancet* **396**, 1644–1652 (2020).

43. Parasassi, T. et al. Low density lipoprotein misfolding and amyloidogenesis. *Faseb J* **22**, 2**350**–2356 (2008).

44. Khoo, J. C., Miller, E., McLoughlin, P. & Steinberg, D. Enhanced macrophage uptake of low density lipoprotein after self-aggregation. *Arteriosclerosis Official J Am Hear Assoc Inc* **8**, 348–358 (1988).

45. Choi, J. et al. The E3 ubiquitin ligase Idol controls brain LDL receptor expression, ApoE clearance, and Aβ amyloidosis. *Sci Transl Med* **7**, 314ra184 (2015).

46. Platt, F. M., Boland, B. & Spoel, A. C. van der. The cell biology of disease: lysosomal storage disorders: the cellular impact of lysosomal dysfunction. *The Journal of Cell Biology* **199**, 723–734 (2012).

47. Davis, O. B. et al. NPC1-mTORC1 Signaling Couples Cholesterol Sensing to Organelle Homeostasis and Is a Targetable Pathway in Niemann-Pick Type C. *Dev Cell* **56**, 260-276.e7 (2021).

48. Moreno-García, A., Kun, A., Calero, O., Medina, M. & Calero, M. An Overview of the Role of Lipofuscin in Age-Related Neurodegeneration. *Front Neurosci-switz* **12**, 464 (2018).

49. Moldavski, O. et al. Lipid Droplets Are Essential for Efficient Clearance of Cytosolic Inclusion Bodies. Dev Cell **33**, 603–610 (2015).

50. Zhao, L. et al. Lanosterol reverses protein aggregation in cataracts. Nature **523**, 607–611 (2015).

51. Makley, L. N. et al. Pharmacological chaperone for α-crystallin partially restores transparency in cataract models. Science 350, 674–677 (2015).

52. Dart, C. SYMPOSIUM REVIEW: Lipid microdomains and the regulation of ion channel function. *J Physiology* **588**, 3169–3178 (2010).

53. Shen, D. et al. Lipid storage disorders block lysosomal trafficking by inhibiting a TRP channel and lysosomal calcium release. Nat Commun 3, 731 (2012).

54. Subramanian, A. et al. Gene set enrichment analysis: a knowledge-based approach for interpreting genome-wide expression profiles. *Proc Natl Acad Sci USA* **102**, 15545–15550 (2005).

55. Mootha, V. K. et al. PGC-1α-responsive genes involved in oxidative phosphorylation are coordinately downregulated in human diabetes. Nat Genet 34, 267–273 (2003).

56. Matyash, V., Liebisch, G., Kurzchalia, T. V., Shevchenko, A. & Schwudke, D. Lipid extraction by methyl-tert-butyl ether for high-throughput lipidomics*s. J Lipid Res 49, 1137–1146 (2008).

57. Melamud, E., Vastag, L. & Rabinowitz, J. D. Metabolomic Analysis and Visualization Engine for LC−MS Data. *Anal Chem* **82**, 9818–9826 (2010).

58. Carmody, W. R. An easily prepared wide range buffer series. *J Chem Educ* **40**, A386 (1961).

59. Schindelin, J. et al. Fiji: an open-source platform for biological-image analysis. *Nat Methods* **9**, 676–682 (2012).